IVYSPRING INTERNATIONAL PUBLISHER

Theranostics

2018; 8(15): 4141-4151. doi: 10.7150/thno.27995

Review

Near-Infrared-II (NIR-II) Bioimaging *via* Off-Peak NIR-I Fluorescence Emission

Shoujun Zhu[1], Bryant C. Yung[1], Swati Chandra[1], Gang Niu[1], Alexander L. Antaris[2]✉, Xiaoyuan Chen[1]✉

1. Laboratory of Molecular Imaging and Nanomedicine, National Institute of Biomedical Imaging and Bioengineering (NIBIB), National Institutes of Health (NIH), 35A Convent Dr, Bethesda, Maryland 20892, United States
2. Intuitive Surgical, Kifer Rd, Sunnyvale, CA 94086, United States

✉ Corresponding author: Email: shawn.chen@nih.gov; Email: alexander.antaris@intusurg.com

Received: 2018.06.19; Accepted: 2018.06.20; Published: 2018.07.16

Abstract

Significantly reduced photon scattering and minimal tissue autofluorescence levels in the second biological transparency window (NIR-II; 1000-1700 nm) facilitate higher resolution *in vivo* biological imaging compared to tradition NIR fluorophores (~700-900 nm). However, the existing palette of NIR-II fluorescent agents including semiconducting inorganic nanomaterials and recently introduced small-molecule organic dyes face significant technical and regulatory hurdles prior to clinical translation. Fortunately, recent spectroscopic characterization of NIR-I dyes (e.g., indocyanine green (ICG), IRDye800CW and IR-12N3) revealed long non-negligible emission tails reaching past 1500 nm. Repurposing the most widely used NIR dye in medicine, in addition to those in the midst of clinical trials creates an accelerated pathway for NIR-II clinical translation. This review focuses on the significant advantage of imaging past 1000 nm with NIR-I fluorophores from both a basic and clinical viewpoint. We further discuss optimizing NIR-I dyes around their NIR-II/shortwave infrared (SWIR) emission, NIR-II emission tail characteristics and prospects of NIR-II imaging with clinically available and commercially available dyes.

Key words: near-infrared-II (NIR-II) bioimaging, NIR dyes, tail emission, cyanine dyes, ICG/IRDye800/IR-12N3

1. Introduction

In recent years, a record number fluorescent contrast agents, molecular probes, and fluorescence imaging systems have entered clinical trials to improve intraoperative visualization of critical anatomical structures [1-3]. Clear delineation of blood/lymphatic vasculature, lymph nodes, nerves and cancerous tissue proves challenging under open and white-light endoscopic viewing conditions. Current biomedical fluorophores span a continuum of wavelengths with emission peaks between 510-840 nm; dyes in the infrared region (NIR-I; ~700-900) generally demonstrate increased imaging penetration depth and signal-to-background ratios given favorable tissue properties compared to visible wavelengths (400-700 nm) [4-6]. Fluorescein (λ_{abs} = 494 nm; λ_{em} = 510 nm) angiography facilitates study of the retina and choroid circulation, providing diagnostic information for various pathologies including diabetic retinopathy. Topical application of FDA-approved Cystview (hexaminolevulinate; 5-ALA derivative) during cystography increases endogenous fluorescent protoporphyrin IX production (λ_{abs} = 405 nm; λ_{em} = 635 nm) and thus enables visualization of nonmuscle invasive papillary bladder cancer [7]. Near-infrared (NIR-I; 700-900 nm) fluorescent angiography with indocyanine green (ICG; λ_{abs} = 805 nm; λ_{em} = 830 nm [in blood]) and infrequently with methylene blue (λ_{abs} = 665 nm; λ_{em} = 691 nm) informs surgeons of perfusion levels and overall tissue health. Subcutaneous ICG injections can additionally identify lymphatic vasculature/node drainage surrounding tumors for fluorometric sentinel lymph node mapping and cancer staging [3]. To expand the limited selection of FDA-approved

fluorescent probes, numerous contrast agents, structure-inherent targeting probes and molecular imaging agents have begun to navigate the regulatory pathway gulfing academic research and medical use, including oral Gleolan (5-ALA), OTL38, IRDye800CW, LUMO15, etc [8-10].

Fluorescence imaging has expanded to near-infrared II (NIR-II, 1000-1700 nm) wavelengths due to reduced scattering (scaling with $\lambda^{-\alpha}$; α = 0.2–4 for most tissues) and minimal autofluorescence in comparison to the well-established visible and NIR-I (700-900 nm) spectral regions [11-15]. Optical spectroscopy of SWCNT/QD tunable semiconducting band structures first unveiled intrinsic fluorescence signal > 1000 nm; in parallel, academic research focused at the intersection of nanoscience and biology highlighted the improved bioimaging metrics achievable with NIR-II nanomaterial fluorophores. Favorable light-tissue interactions within the near-infrared II (oftentimes termed shortwave infrared or SWIR) spectrum have produced unparalleled non-invasive optical access through the intact skin/scalp to ~4 mm depths into the murine cerebral cortex, fluorescent tumor-to-normal tissue signal ratios ~2-4-fold higher than identical targeting moieties coupled to NIR-I probes, and 10-fold higher lymph node signal-to-background ratios (SBR) compared to the traditional infrared region. Until 2016, NIR-II fluorophores comprised entirely of nanomaterials such as single-walled carbon nanotubes (SWCNTs) [13, 16-22], quantum dots [23-27], and rare earth-doped nanoparticles [28-31]. Unfortunately, current inorganic nanomaterial fluorophores raise critical safety concerns due to their retention and accumulation in the liver/spleen post-imaging and potential immunogenic responses. The lack of NIR-II fluorophores with high brightness and suitable pharmacokinetics presented a major bottleneck in the path towards clinical adoption of NIR-II fluorescence imaging [32].

To overcome inherent limitations in nanomaterial probes, researchers endeavored to synthesize/optimize organic small-molecule NIR-II dyes with improved excretion profiles and reduced toxicity concerns. Fortuitously, NIR-II organic probe designers found inspiration in varied realms of research including organic solar cells, organic LEDs, dye-pumped laser gain mediums, and organic electronics that all required small molecules with > 1000 nm fluorescent emission for their individualized applications [33]. The most promising dye architecture, based on an electron donor–acceptor–donor (D-A-D) motif with highly tunable emission between 900–1600 nm, resulted in several high-performance D-A-D NIR-II fluorophores (CH1055) with ~90% renal excretion [34-36]. More recent NIR-II organic dyes such as CH-4T introduce new strategies to boost quantum yield through formation of dye-protein molecular complexes, yielding a fluorophore 36-fold brighter than initial PEGylated NIR-II organic dyes [37]. Although rapidly progressing towards an idealized NIR-II dye, clinical translation will require further efforts in fundamental probe chemistry to synthesize a strong clinical candidate with high quantum yield, large absorption coefficient, aqueous solubility, functional groups for covalent targeting moiety labeling, and favorable pharmacokinetics.

Interestingly, recent spectroscopic characterization of NIR-I cyanine dyes revealed long emission tails that stretch into the NIR-II region past 1500 nm, opening an entirely new route to clinical NIR-II imaging [37-40]. Disparate photospectrometer behavior in the region separating silicon's (NIR-I sensor active layer) falling quantum efficiency (QE) and InGaAs's (NIR-II sensor active layer) rising QE near 1000 nm has underreported the NIR-II emission of FDA-approved NIR-I dyes. Clinical NIR imaging relies almost exclusively on indocyanine green (ICG) with the polymethine IRDye800CW pulling ahead as one of the most promising conjugatable NIR-I candidates in clinical trials [41]. Indocyanine green (ICG), approved by the U.S. Food & Drug Administration (FDA) in 1959, has been extensively adopted for clinical angiography and perfusion assessment in open, laparoscopic and robotic surgery [42]. The high quantum yield of these NIR-I dyes coupled with excellent pharmacokinetic profiles makes both dyes well suited for biomedical imaging at > 1000 nm. In this review, we focus on the intriguing new possibilities of NIR-II imaging with NIR-I peak dyes from both clinical and theoretical vantages. Further, we discuss synthetic strategies/ chemical structures, dwindling NIR-II emission tails, and advantages of NIR-II image-guided surgery. Finally, we discuss the feasibility of leveraging the NIR-II emission of FDA-approved ICG, clinical IRDye800CW and commercial IR-12N3 for deep-tissue biomedical imaging.

2. NIR-II molecular fluorophores

The first aqueous NIR-II small-molecule dye (CH1055-PEG) consisted of a donor-acceptor-donor (D-A-D)-type architecture based off a similar dye class found in organic NIR LED applications (Fig. 1) [33, 43-46]. Donor-acceptor-donor chromophores are particularly interesting NIR-II fluorescent probes given their disposition to systematic molecular rearrangement [47]. These dyes consist of a central benzo[1,2-c:4,5-c']bis([1,2,5]thiadiazole) (BBTD) moi-

ety, a strong electron withdrawing heterocyclic quinoid, flanked on either side by strong electron donors. These electron donating groups are molecularly wired to the central BBTD electron acceptor through aromatic π-bridging linkers, yielding increased electron delocalization and low energy gaps capable of NIR-II emission [48]. CH1055-PEG enabled high-resolution visualization of murine peripheral and cerebral vasculature, excellent tumor-to-background signal ratios, and renal excretion levels > 90%. CH1055-PEG's quantum yield of 0.03%, measured using IR26 as a reference fluorophore with a quantum yield of 0.05% in DMSO,

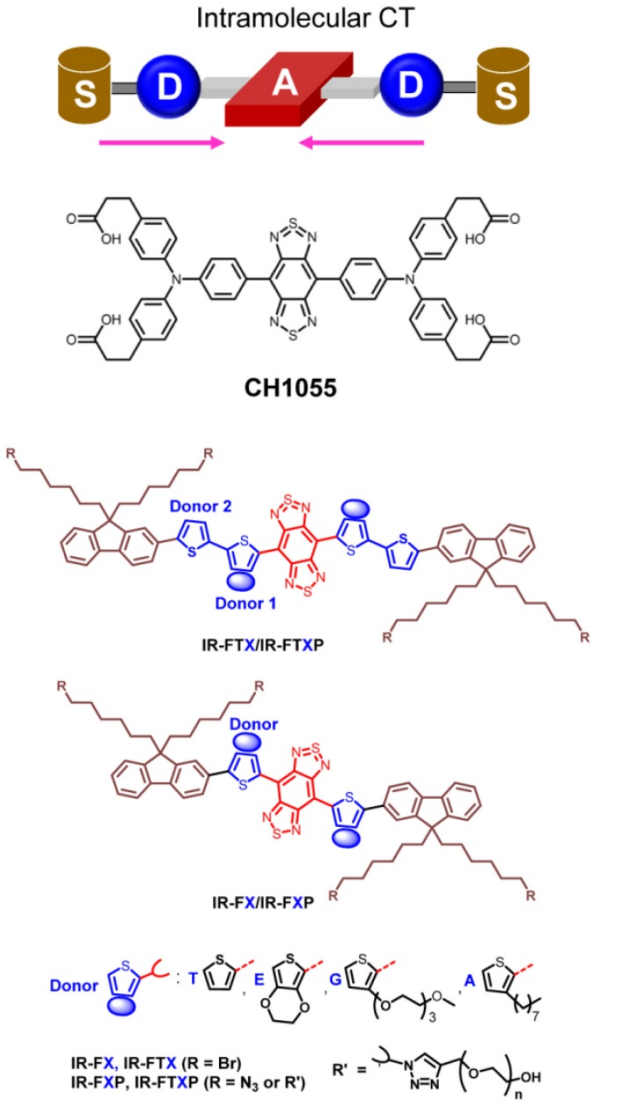

Figure 1. Schematic illustration of donor-acceptor-donor (D-A-D) molecular fluorophore design. A PEGylated CH1055, the first water-soluble NIR-II dye with D-A-D structure, served as the structural basis for systematic rearrangement for increasing quantum yield [34]. BBTD serves as the acceptor unit with modified thiophene functioning as the bridging donor unit. The modified thiophene close to BBTD can distort the conjugated backbone and increase the dihedral angle between BBTD and thiophene to increase quantum yield. Further, dialkyl chains substituted fluorene units can function as the shielding units as the stretching dialkyl chains out of the conjugated backbone plane could efficiently prevent parallel intermolecular interactions. Reprinted with permission from Ref. [51], copyright 2018 American Chemical Society.

produced sufficient fluorescence intensity for enhanced biomedical imaging in the NIR-II spectral region [49]. However, discrepancies in the reported quantum yield of IR26 (QY = 0.05%, 0.1%, 0.5%) and the dearth of well characterized reference fluorophores spanning 1000-1700 nm make precise NIR-II dye quantum yield characterization difficult [50]. Fundamentally different sensor technology between the first and second biological transparency window (silicon for visible/NIR-I and InGaAs for NIR-II) further complicates quantum yield measurements. Fortunately, relative brightness differences among fluorophores within the NIR-II field still hold while a consensus on IR-26's quantum yield value will only scale absolute quantum yield values of the entire NIR-II field.

Subsequent efforts systematically tuned CH1055's electron donating moieties, π-bridging linkers, and terminal functional groups to boost quantum yield. Disparate strategies to increase brightness focused either on increasing intramolecular charge transfer, improving molecular rigidity, or dye complexation with serum proteins such as human serum albumin (HSA). Introduction of shielding groups (S) at the dye terminus produced an S-D-A-D-S structure, protecting the dye's backbone from both intermolecular interactions and fluorescence-quenching aggregation. Further, both theoretical simulations and experimental results showed that an 3,4-ethylenedioxy thiophene electron donor distorts the conjugated backbone and tunes the electrostatic distribution, protecting the BBTD acceptor in the excited state. The quantum yield of these D-A-D dyes gradually increased from the first generation CH1055-PEG to IR-FGP (QY = 0.2%; IR26 = 0.05%, DMSO) through molecular engineering [52]. Notably, the molecular fluorophore IR-FTAP with octyl thiophene as the first donor and thiophene as the second donor exhibits fluorescence emission peaked at 1048 nm with a QY of 0.53% (IR26 = 0.05%, DMSO) in aqueous solutions (Fig. 1) [51]. The carboxylated CH1055 demonstrated poor aqueous solubility, thus requiring PEGylation prior to intravenous injection [53, 54]. However, replacement of terminal carboxylic acid functional groups with sulfonic acid realized a fully water soluble NIR-II dye termed CH-4T. Expecting similar *in vivo* brightness levels as CH1055-PEG after intravenous injection, murine models injected with CH-4T resulted in a brilliant increase in fluorescent intensity by nearly two orders of magnitude. Further investigation into this phenomenon revealed CH-4T formed supramolecular assemblies with serum proteins such as albumin and lipoproteins after injection into the bloodstream. CH-4T binding to protein hydrophobic pockets/

regions increased the dye's fluorescent brightness by nearly 110-fold (QY = 1.1%; IR26 = 0.05%, DMSO), ultimately producing by the brightest fluorophore with emission between 1000-1300 nm [37]. Unfortunately, this increase in quantum yield eliminated renal excretion and slowed the pharmacokinetic excretion profile significantly.

Innovative new approaches to red-shifting the fluorescence emission of existing infrared polymethine dyes recently produced a new SWIR-emissive dye class with both a high quantum yield and absorbance coefficient (ε) [55, 56]. Through increasing the conjugation length separating the electron donor/acceptor and heteroatom substitutions, a few commercially-available polymethine molecules such as IR-1040, IR-1048, IR-1051, and IR-1061 can fluoresce over 1000 nm [57, 58]. In a departure from solely increasing the polymethine chain length, a proven method of red-shifting cyanine dyes, Cosco *et al.* extended the heterocycle conjugation and added new electron donating groups (Fig. 2) [55]. These innovative flavylium polymethine NIR-II fluorescent agents, with peak emission wavelengths > 1000 nm, show quantum yields exceeding 0.53% (IR26 = 0.05%, DMSO) along with high absorption coefficients surpassing 236,000 ($M^{-1}cm^{-1}$). This represents the first attempt to systematically tune the NIR-II quantum efficiency value (QE), a dye metric encompassing both the quantum yield and absorption coefficient (QE = ε*QY). Most of the above-mentioned organic NIR-II fluorophores are organic-phase products with low aqueous solubility, and require encapsulation in a hydrophilic matrix for live imaging. Very recently, Li *et al.* developed a novel small molecule fluorophore FD-1080 with both excitation/emission in NIR-II region through a structural re-design of typical cyanine dyes. The sulfonated FD-1080 possesses good water solubility and high quantum yield (QY of complex = 5.94%; IR26 = 0.05%, DMSO) via protein binding. More importantly, FD-1080 demonstrates increased photostability with respect to both ICG and IRDye800CW [59].

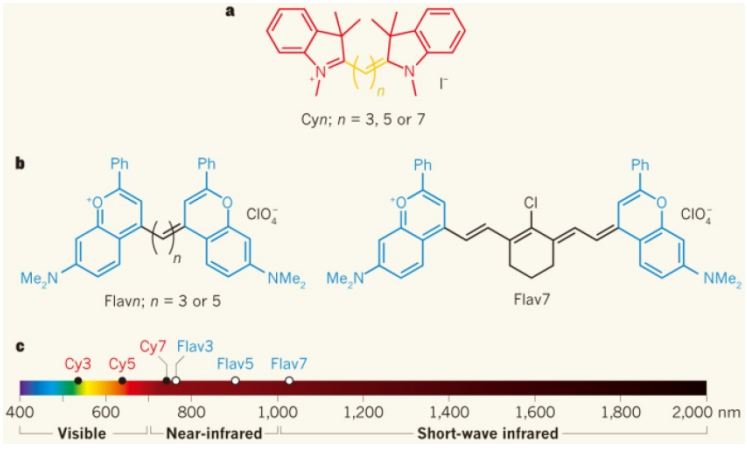

Figure 2. Through increasing the conjugation length separating the electron donor/acceptor and heteroatom substitutions, the polymethine molecules can fluoresce over 1000 nm, reported by Cosco et al.[55] a) The Cyanine (Cy) dye series of compounds is used for optical fluorescence imaging. b) Flavylium polymethine fluorophores were developed by replacing the indolenines with dimethyl-flavylium heterocycles (blue). c) Flav7 emits and absorbs light in NIR-II window. Reprinted with permission from Ref. [32, 55].

3. NIR-I fluorophores with NIR-II emission tails

Fluorescent dyes possess relatively broad emission peaks with photon energies spanning large regions of the electromagnetic spectrum. Underlying tissue optical properties vary as a function of optical wavelength; thus fluorescent emission sub-bands may improve upon imaging metrics due to reduced scattering at progressively longer wavelengths. For instance, NIR-II (1,000-1,700 nm) division into the NIR-IIa (1,300-1,400 nm) and NIR-IIb (1,500-1,700 nm) improves optical penetration depths in contrast to imaging between 1,000-1,200 nm [34, 60]. Oftentimes, simply changing fluorescent imaging filter sets (short/long pass filters) to capture longer wavelength photons while maintaining sufficient detector counts markedly increases imaging performance. For instance, imaging in these NIR-II sub regions is often achieved by selecting longer wavelength photons from shorter peak emission semiconducting nanomaterials [34]. Regardless of a dye's peak emission wavelength, division of fluorescent signal into discrete bands provides a reliable strategy for optimizing biomedical imaging performance. Recent spectroscopic investigation of NIR-I peak dyes, many of which possess broad emission ranges with a full width at half max > 100 nm, have highlighted their potential for NIR-II biomedical imaging.

Recent characterization using InGaAs spectrometers of high quantum efficiency NIR-I dyes, including the ICG (822 nm peak emission), IRDye800 (789 nm peak emission) and IR-12N3 (~800 nm peak emission), revealed long NIR-II emission tails extending beyond 1500 nm [37, 38, 40]. Surprisingly, off-peak fluorescent signal in the NIR-II window produced comparable brightness levels to early-generation D-A-D dyes, realizing improved optical imaging metrics characteristic of NIR-II imaging yet with dyes already found in clinical or preclinical settings (Fig. 3a-b) [37, 38]. The Franck-Condon principle indicates that emission spectra of most fluorescent dyes should approximate the mirror image of the absorption spectra; however, previous optical characterization on silicon spectrometers neglected and falsely

reported fluorescent emission of NIR-I dyes due to negligible silicon detector efficiency past ~ 1000 nm (Fig. 3c-d). Although recent sulfonated D-A-D structured NIR-II dyes seem to surpass both the SWIR fluorescent brightness of early-generation NIR-II fluorophores as well as NIR-II signal from ICG/IRDye800CW/IR-12N3 [37, 55], these ground-breaking results provide a straightforward path to clinical NIR-II imaging. Furthermore, these findings require the fluorophore chemistry community to revisit optical characterization methodologies of ~1000 nm-emitting dyes that straddle regions of both low silicon and InGaAs detection quantum efficiency. Regardless, ICG/IRDye800CW/IR12-N3's remarkable NIR-II emission tail provides the potential for rapidly transitioning NIR-II imaging into the operating room.

High quantum yield NIR-I dyes with long emission tails reaching into the NIR-II/SWIR provides a new synthetic approach for biomedical NIR-II imaging. Although optimization and discovery of NIR-II peak dyes should continue in parallel, development of bright, NIR-I dyes with strong NIR-II emission provides a relatively unexplored route towards imaging past 1000 nm. NIR-I fluorophores mostly display high quantum yields (~5-30%) while the vast majority of NIR-II dyes suffer from lower quantum yields with a few notable exceptions (*e.g.*, CH-4T [37], flavylium polymethines [55, 59]) given the propensity of non-radiative electron/hole recombination in low energy-gap molecules; thus, red-shifting high quantum yield NIR-I dye architectures for NIR-II tail optimization provides a unique approach for NIR-II bioimaging. For instance, Qi et al. recently reported an NIR aggregation induced emission luminogen (AIEgen) with a fluorescent peak in the NIR-I region (800 nm) yet whose emission spans across 700-1200 nm. AIEgen displayed a high quantum yield NIR-II tail emission (QY > 900 nm = 0.28%, IR26=0.05%, DMSO) (Fig. 3e-f) [61]. By forming biocompatible NIR-AIE-dots with Pluronic F-127, real-time and high-resolution imaging in the NIR-II/SWIR spectral region was observed in murine tumor and brain models. Xu et al. also developed an activatable NIR-II nano-probe for visualizing colorectal cancers using the off-peak emission of boron-dipyrromethene (ZX-NIR) dye in NIR-II region [62]. Although this provides a new synthetic approach for preclinical NIR-II emission tail optimization, careful optical spectroscopy of NIR-I peak dyes undergoing both feasibility and phase I/II/II clinical trials (e.g., ZW800-1, IS001, IRDye800 derivatives) could potentially reveal stronger NIR-II emission tails than ICG/IRDye800CW/IR-12N3.

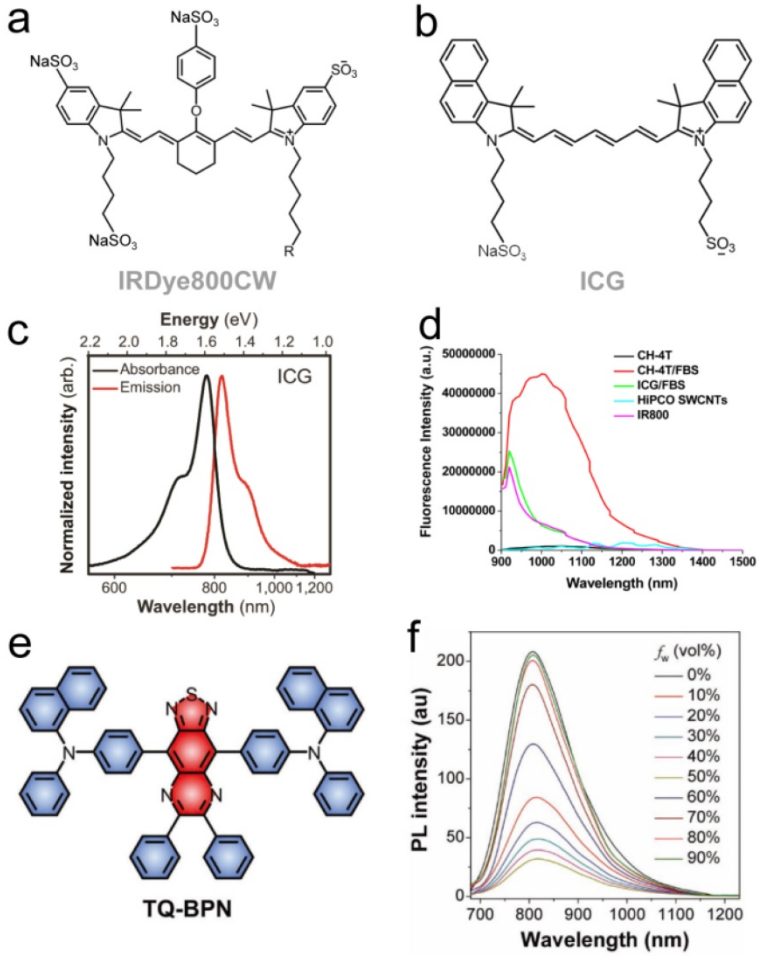

Figure 3. NIR-II biomedical imaging with FDA-approved ICG and IRDye800CW. a-b) Chemical structures of IRDye800CW and ICG. c) Fluorescent emission spectra of NIR-I dyes captured on InGaAs photospectrometers: the silicon detector measures artificially reduced emission tails due to their low efficiency in SWIR region, while InGaAs detectors recover the true emission tail [38]. d) Fluorescent emission spectra of NIR-I/II dyes past 900 nm. e) Molecular structure of NIR AIEgen (TQ-BPN). f) PL spectra of TQ-BPN in THF/H_2O mixtures with different water fractions (f_w). Reprinted with permission from Ref. [38] for c), Ref. [37] for d), and Ref. [61] for e-f).

4. NIR-II imaging with IRDye800CW

IRDye800CW's combination of high quantum yield (QY = ~12% in serum) and functional groups for facile targeting moiety bioconjugation have propelled IRDye800CW to the forefront of clinical near infrared fluorescent dyes [12]. IRDye800CW is ideal for protein/antibody labeling with NHS ester, maleimide, carboxylate, DBCO, azide, and alkyne forms available. LICOR's IR800BK pharmacokinetics demonstrates excellent renal excretion, enabling fluorescent visualization of the ureter, an anatomical structure that sustains frequent

iatrogenic transection. The superior optical and pharmacokinetic properties have spurred ~15 recent U.S.-based clinical trials in various phases of completion that center mainly on improved cancer visualization. Notable examples include therapeutic antibody (*i.e.,* panitumumab/cetuximab) conjugation to 1-2 dye molecules, realizing targeted optical probes that display similar pharmacokinetic/toxicology profiles to the unmodified antibody. This unique approach leverages commercial, FDA-approved antibodies capable of targeting wide ranging cancer types as tumor-specific targeting ligands. Successful clinical trial results with panitumumab/cetuximab-IRDye800CW conjugates for targeted head and neck squamous cell carcinomas (HNSCC) produced clear cancer margin delineation with tumor-to-background ratios surpassing 3-4 [63, 64]. Furthermore, interest in newly-developed multimodal probes coupling PET and fluorescence imaging (*e.g.,* ^{68}Ga-bombesin-IRDye800CW) facilitate 3D tomographic PET models for pre-surgical planning while providing real-time fluorescent image-guidance during tumor/lymph node resection [65]. These dual-modality probes have broad-spectrum potential for improving outcomes in a diverse cancer patient population.

IRDye800CW optical characterization by Alexander and Carr *et al.* on InGaAs sensors revealed the existence of long emission tails extending into the SWIR/NIR-II region [37, 38]. In comparison to IR-E1050 (QY = 0.2%; IR26 = 0.05%), an early generation dye with 1050 nm peak fluorescence emission, IRDye800CW displayed 3.8-fold and 1.3-fold higher brightness between 1000-1620 nm and 1300-1620 nm, respectively. Imaging at > 1000 nm on InGaAs detectors produces significantly sharper/crisper images than the traditional IRDye800CW imaging region on silicon detectors (800-900 nm) as longer wavelength NIR-II/SWIR subdivisions yield improved metrics due to progressively reduced scattering and autofluorescence levels [38]. As demonstrated by Hong *et al*, the sub-window spanning 1300-1400 nm (termed the NIR-IIa) allowed non-invasive mouse cerebral cortex visualization through the intact skin/skull in comparison to a 1000-1200 nm sub-window which disallowed clear discrimination of murine cerebral vasculature [17, 60]. The off-peak NIR-II fluorescence from IRDye800CW produced sufficient fluorescent signal > 1150 nm to clearly highlight a BT474-Gluc tumor underneath the murine skin/skull when targeted with an IRDye800CW-trastuzumab conjugate [38]. Due to the fact that molecular imaging in NIR-II window reaches the tumor-to-normal tissue ratio as high as 12 (Fig. 4), IRDye800CW's fluorescent signal strength across various NIR-II sub-windows could instantaneously increase detection depths and resection precision levels with the relatively simple incorporation of InGaAs sensor technology into clinical infrared imaging platforms.

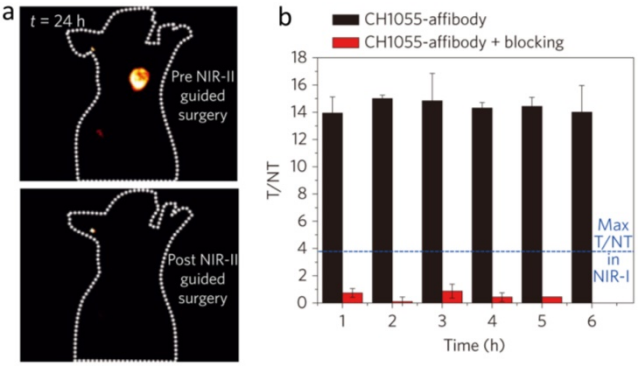

Figure 4. Advantage of molecular imaging in NIR-II window compared with NIR-I window. a) Images of a mouse before and after performing NIR-II fluorescence image-guided surgery to excise the tumor. b) Tumor-to-normal tissue ratios obtained for the CH1055-affibody during targeting and blocking. Blue line demarcates the T/NT ratio obtained with NIR-I fluorophores with the same affibody. Reprinted with permission from Ref. [34], copyright 2016 Nature Publishing Group.

5. NIR-II imaging with FDA-approved ICG

Similarly to IRDye800CW, ICG was found to have an emission shoulder extending into the NIR-II region yet with markedly stronger fluorescent intensity than IR-E1050 [38, 39]. ICG NIR-II/SWIR *in vivo* fluorescence imaging at > 1300 nm increased brain vasculature contrast by ~1.4-fold versus the traditional NIR-I region even with the thick-scalp NU/NU mouse model [38]. The apparent width of a brain vessel decreased from 430 μm to 210 μm when transitioning from the first to second biological transparency window. Furthermore, ICG imaging improved hindlimb arterial/venous/lymphatic vasculature resolution and sacral/popliteal lymph node clarity while simultaneously achieving sufficiently high spatial/temporal resolution for recording heart pulsations through the chest wall (Fig. 5).

Clinical NIR-I imaging with ICG has already offered exquisite sensitivity for non-invasive blood perfusion assessments, liver tumor/metastasis delineation, and lymphatic vasculature/node detection, improving performance in a myriad of surgical tasks [66]. The high ICG NIR-II fluorescent signal could immediately benefit all of these surgical applications by enhancing the surgeon's ability to precisely resolve deep anatomical features. Although ICG does not contain any functional groups for covalent conjugation to targeting moieties, innovative administration strategies can produce selective dye

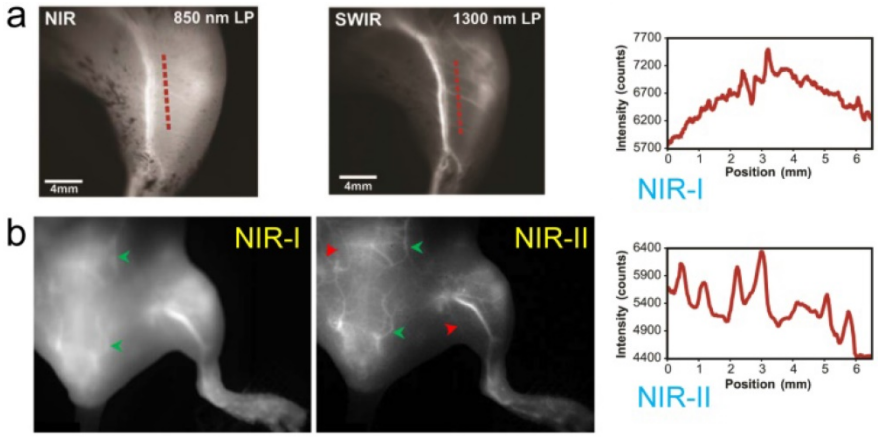

Figure 5. NIR-II imaging of both NIR-II and NIR-I fluorophores offer higher resolution and visualization of deep tissue than can be achieved using visible/NIR-I fluorescence imaging. a) The hind limb vessels imaging and cross-sectional fluorescence intensity profiles (NIR-II) along red-dashed lines of a mouse injected with ICG were taken at NIR-I and NIR-II windows, respectively. b) The hind limb vessels imaging of a mouse injected of ICG were taken at NIR-I and NIR-II windows, respectively. Reprinted with permission from Ref. [38] for a), Ref. [39] for b).

accumulation in target structures. For instance, hepatocellular carcinomas that disrupt ICG biliary clearance routes show selective ICG accumulation after intravenous injection multiple days prior to surgery. Similarly, subdermal cervical ICG injections demarcate lymphatic drainage pathways for fluorescence-guided lymph node removal in endometrial cancer, a high-benefit therapeutic surgical approach for cancer staging backed up by strong clinical evidence. These current ICG surgical uses as a non-targeted contrast agent could immediately benefit from the minimized feature broadening and lower background autofluorescence levels in the NIR-II region. Furthermore, new molecular imaging agents in clinical trials include a cancer-targeting alkylphosphocholine analogue (CLR1502 targeting breast/brain cancers) as well as a tumor ligand chlorotoxin that both utilize ICG (or very close structural derivatives) as a fluorescent probe [2]. These exciting new ICG-based molecular imaging agents provide a promising route for precision NIR-II fluorescent imaging [39].

6. NIR-II imaging with IR-12N3

Besides FDA-approved ICG and clinical-trail IRDyed800CW, there are various commercial dyes fluorescing in NIR-I region. With systematically investigating the off-peak emission of the NIR-I dyes (cyanine dyes, CF dyes, DyLight Benzopyrillium dyes, Alexa Fluor dyes), Zhu et al. screened another bright NIR-I dye, IR-12N3 (a re-designed cyanine dye produced by Nirmidas biotech), with both super bright NIR-I peak and NIR-II tail emission [40]. The NIR-I fluorescence quantum yield of IR-12N3 in serum was found 3 and 2 times higher than ICG and IRDye800 respectively. Using IR-12N3's outstanding emission-tail brightness in NIR-II region, NIR-II deep tissue imaging of targeting organs and tumors were achieved with super contrast and high signal-to-background ratio (SBR) in mouse model compared with NIR-I imaging of the same contrast agent. The administrated IR-12N3 in blood vascular system of mouse body affords extremely clear vessel imaging (Fig. 6a) and deep lymph node imaging. Although the imaging time window is short (in 2 min) due to short circulation time of NIR-12N3, it still affords a tunable platform for optimizing both contrast and speed in fluorescence guided surgery. The targeted NIR-II imaging based on IR-12N3@antibody conjugate enhances the tumor to normal tissue ratio (TNR) from ~4 of NIR-I window to ~10 of NIR-II window (Fig. 6b), showing promise for aiding cancer localization and intraoperative surgical margin assessment. The photophysical mechanism of tail emission in the present NIR-I dyes was also clarified: the rotation of middle C-C bridge bonds of cyanine can destroy the symmetries of π-conjugated backbone; then the asymmetry of π domain in S1 state of NIR-I dyes results in the twisted intramolecular charge transfer (TICT) process; the TICT S_1 state is very sensitive to the surrounding environment, resulting in both strong NIR-II emission and enhancement in serum buffer (Figure 6c). The established emission mechanism provides a general rule for guiding future NIR-I/II fluorophore synthesis. However, detailed reasons for NIR-II tail emissions require further investigation from multiple angles including electronic/vibronic transitions, solvation, and cumulative emission.

7. Pharmacokinetics of NIR-II fluorescent agents

Although preclinical NIR-II peak dyes (*e.g.*, CH1055-PEG, IR-E1) have recently demonstrated suitable renal clearance levels [34, 35], subsequent efforts to improve quantum yield have hampered their excretion profile (*e.g.*, CH-4T) [37]. For successful NIR-II clinical translation, fluorophores must clear from the body with minimum retention in blood/organs post-imaging. Due to high plasma protein binding affinity, ICG's excretion pathway relies exclusively on the hepatobiliary system [67]. IRDye800CW demonstrates a renal-excretion pathway, owing to high serum stability, low molecular weight, and minimal protein complexation

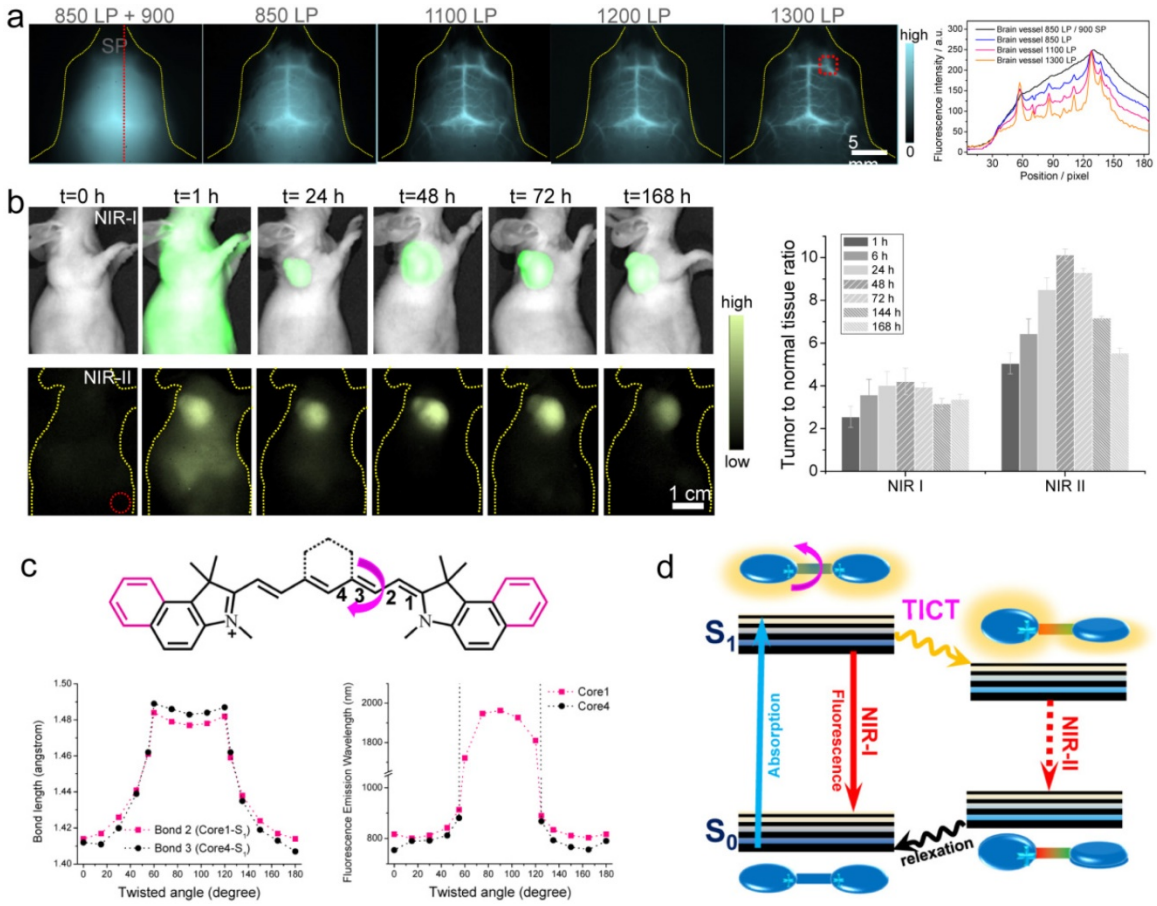

Figure 6. NIR-II imaging with tail emission of IR-12N3. a) Brain vessel imaging with IR-12N3 at different NIR-I and NIR-II sub-windows. Right figure shows fluorescent cross-sectional intensity profile of brain vessel in both NIR-I and NIR-II windows. b) Targeting tumor imaging under NIR-I/II windows and corresponding tumor-to-normal tissue ratios of IR-12N3@Erbitux treated SCC tumor bearing mice. c) Core structures of ICG (core 1) and IRDye800/IR-12N3 (core 4); Below profiles show the calculated bond lengths of bond 2 of core 1 and bond 3 of core 4 as a function of twisted angles (left) as well as simulated fluorescence emission wavelength of core 1 and core 4 as a function of twisted angles (right). d) Schematic illustration of the origin of emission tail and TICT proposed in NIR-I dyes. Reprinted with permission from Ref. [40].

[68]. The excretion behavior of these dyes follows the established rule that small and hydrophilic molecules are mainly excreted via the kidneys, whereas large and amphipathic molecules are preferentially excreted via the liver [67]. Investigation into the relationship between NIR-II chemical structure and excretion mechanism can draw on many of the design principles based on NIR-I fluorophore chemistry.

Although NIR-II emission of NIR-I dyes should accelerate clinical translation of NIR-II imaging, there are still limitations of current NIR-II fluorophores. For example, IRDye800CW and other cyanine dyes, like Cy7, Cy7.5 suffer from the nonspecific skin accumulation, potentially making noninvasive fluorescence imaging challenging [40, 69]. When calculating background levels in tumor-to-background metrics, tissue background includes both autofluorescence level and non-specific accumulation. As a result, to decrease non-specific background levels, many innovative strategies including zwitterion charge distributions could improve NIR-II peak dye biomedical imaging metrics [69]. Choi et al. exploited zwitterionic ZW800 (which may pertain an inherent NIR-II emission tail) with a reduction in the net charge of the molecule [70-72]. Owing to charge shielding effects resulting from the charge-neutral structural design, the zwitterionic ZW800 afford much higher signal to background ratio compared NIR fluorophores with net charges [70].

The most promising NIR-II dye architecture, based on an electron D-A-D motif with highly tunable emission between 900–1600 nm, resulted in several high-performance D-A-D NIR-II fluorophores with renal excretion ability [34-36]. These NIR-II organic dyes combined the improved imaging performance as expected at progressively longer imaging wavelengths with the favorable pharmacokinetic excretion profile of small molecules. Besides organic NIR-I/II dyes for NIR-II window bioimaging, ultrasmall luminescent inorganic nanoparticles or nanoclusters, with large surface/volume ratios, tunable and diverse material properties, are potential choices for preclinical/clinical using [73, 74]. For example, Zhou et al. developed ultrasmall Au nanoparticles with efficient renal clearance with not only low RES uptake and high biocompatibility but

also passive tumor targeting capability [74]. Furthermore, the biodegradable nanomaterials afford another direction for developing clinically potential NIR-II fluorophores. However, there is still long way to translate such newly-developed fluorophores into clinical use.

8. Conclusion and outlook

We anticipate that NIR-I dyes will see extensive use as NIR-II fluorescent probes, particularly in translational and clinical studies wherein surgeons need to recognize tumor margin and intricate anatomical structures. ICG/IRDye800CW's NIR-II emission opens a new route for translational infrared imaging in the second biological transparency window that does not require extensive NIR-II-peak fluorophore toxicology profiles and FDA investigation new drug (IND) applications. The incorporation of InGaAs detectors into silicon-based fluorescence imaging systems can support clinical imaging platforms with broad-spectrum capabilities for improving surgical outcomes and ultimately enhancing patient care.

Although NIR-I dyes provide a straightforward path to NIR-II clinical translation, researchers still need to develop efficient peak NIR-II dyes to complement the existing library of peak NIR-II preclinical candidates [75]. Newly-developed NIR-II dyes with elevated quantum yields and extinction coefficients will require clinical assessment to address toxicity and safety concerns; however, these efforts are merited for a high brightness NIR-II fluorescent candidate. The last few years have seen the first peak NIR-II organic dye (CH1055) followed by a 160-fold increase in quantum yield resulting in FD-1080 (QY = 5.94%; IR26 = 0.05%) [34, 59]. Further efforts will likely result in progressively brighter NIR-II peak dyes; however, parallel progress through NIR-II emission tail optimization should expedite the development of bright, conjugatable NIR-II emissive imaging agents.

Although NIR-II fluorescence imaging significantly improves penetration depth and resolution, optical imaging cannot peer into the body beyond ~ centimeters depth. Multimodality imaging probes, achieved through advanced fluorophore conjugates to MR/US/PET probes, is an efficient route to solve the penetration limit of optical imaging. For instance, PET-NIR dye conjugates (*e.g.*, ^{68}Ga-bombesin-IRDye800CW [65], ^{64}Cu-DOTA-trastuzumab-IRDye800CW [76]) provide preoperative tomographic PET cancer/metastases detection in addition to real-time, intraoperative fluorescent guidance. Selecting NIR-I dyes with long, NIR-II emission tails for multimodal probes would allow surgeons to toggle between various NIR-I/II sub-bands depending on surgical tasks. The integrated theranostic platforms of the future will include accurate preoperative diagnosis, such as radioscintigraphy and ultrasonography, intraoperative NIR-I/II fluorescence-guided surgery, as well as postoperative monitoring [77-79].

Acknowledgements

This work was supported by the intramural research program of the National Institute of Biomedical Imaging and Bioengineering (NIBIB), National Institutes of Health (NIH).

Competing Interests

The authors have declared that no competing interest exists.

References

[1] Hyun H, Owens EA, Wada H, et al. Cartilage-Specific Near-Infrared Fluorophores for Biomedical Imaging. Angew Chem Int Ed. 2015; 54: 8648-52.
[2] Miao Q, Xie C, Zhen X, et al. Molecular afterglow imaging with bright, biodegradable polymer nanoparticles. Nat Biotechnol. 2017; 35: 1102-10.
[3] Vahrmeijer AL, Hutteman M, van der Vorst JR, et al. Image-guided cancer surgery using near-infrared fluorescence. Nat Rev Clin Oncol. 2013; 10: 507-18.
[4] Blau R, Epshtein Y, Pisarevsky E, et al. Image-guided surgery using near-infrared Turn-ON fluorescent nanoprobes for precise detection of tumor margins. Theranostics. 2018; 8: 3437-60.
[5] Elmire Hartmans, Jolien J.J. Tjalma, Matthijs D. Linssen, et al. Potential Red-Flag Identification of Colorectal Adenomas with Wide-Field Fluorescence Molecular Endoscopy. Theranostics. 2018; 8: 1458-67.
[6] Fujimoto S, Muguruma N, Okamoto K, et al. A Novel Theranostic Combination of Near-infrared Fluorescence Imaging and Laser Irradiation Targeting c-KIT for Gastrointestinal Stromal Tumors. Theranostics. 2018; 8: 2313-28.
[7] Witjes JA, Douglass J. The role of hexaminolevulinate fluorescence cystoscopy in bladder cancer. Nat Clin Pract Urol. 2007; 4: 542-9.
[8] Stummer W, Pichlmeier U, Meinel T, et al. Fluorescence-guided surgery with 5-aminolevulinic acid for resection of malignant glioma: a randomised controlled multicentre phase III trial. The Lancet Oncology. 2006; 7: 392-401.
[9] De Jesus E, Keating JJ, Kularatne SA, et al. Comparison of Folate Receptor Targeted Optical Contrast Agents for Intraoperative Molecular Imaging. Int J Mol Imaging. 2015; 2015: 469047.
[10] Shum CF, Bahler CD, Low PS, et al. Novel Use of Folate-Targeted Intraoperative Fluorescence, OTL38, in Robot-Assisted Laparoscopic Partial Nephrectomy: Report of the First Three Cases. J Endourol Case Rep. 2016; 2: 189-97.
[11] Smith AM, Mancini MC, Nie S. Bioimaging: second window for in vivo imaging. Nat Nanotechnol. 2009; 4: 710-1.
[12] Hong G, Antaris AL, Dai H. Near-infrared fluorophores for biomedical imaging. Nat Biomed Eng. 2017; 1: 0010.
[13] Welsher K, Sherlock SP, Dai H. Deep-tissue anatomical imaging of mice using carbon nanotube fluorophores in the second near-infrared window. Proc Natl Acad Sci U S A. 2011; 108: 8943-8.
[14] Jiang Y, Upputuri PK, Xie C, et al. Broadband Absorbing Semiconducting Polymer Nanoparticles for Photoacoustic Imaging in Second Near-Infrared Window. Nano Lett. 2017; 17: 4964-69.
[15] Wang R, Zhang F. NIR luminescent nanomaterials for biomedical imaging. J Mater Chem B. 2014; 2: 2422-43.
[16] Welsher K, Liu Z, Sherlock SP, et al. A route to brightly fluorescent carbon nanotubes for near-infrared imaging in mice. Nat Nanotechnol. 2009; 4: 773-80.
[17] Hong G, Lee JC, Robinson JT, et al. Multifunctional in vivo vascular imaging using near-infrared II fluorescence. Nat Med. 2012; 18: 1841-6.
[18] Antaris AL, Robinson JT, Yaghi OK, et al. Ultra-low doses of chirality sorted (6,5) carbon nanotubes for simultaneous tumor imaging and photothermal therapy. ACS Nano. 2013; 7: 3644-52.

[19] Graf A, Tropf L, Zakharko Y, et al. Near-infrared exciton-polaritons in strongly coupled single-walled carbon nanotube microcavities. Nat Commun. 2016; 7: 13078.
[20] Roxbury D, Jena PV, Shamay Y, et al. Cell Membrane Proteins Modulate the Carbon Nanotube Optical Bandgap via Surface Charge Accumulation. ACS Nano. 2016; 10: 499-506.
[21] Bonis-O'Donnell JTD, Page RH, Beyene AG, et al. Dual Near-Infrared Two-Photon Microscopy for Deep-Tissue Dopamine Nanosensor Imaging. Adv Funct Mater. 2017; 27: 1702112.
[22] Gong H, Peng R, Liu Z. Carbon nanotubes for biomedical imaging: the recent advances. Adv Drug Deliv Rev. 2013; 65: 1951-63.
[23] Zhang Y, Hong G, Zhang Y, et al. Ag_2S quantum dot: a bright and biocompatible fluorescent nanoprobe in the second near-infrared window. ACS Nano. 2012; 6: 3695-702.
[24] Hong G, Robinson JT, Zhang Y, et al. In Vivo Fluorescence Imaging with Ag2S Quantum Dots in the Second Near-Infrared Region. Angew Chem Int Ed. 2012; 124: 9956-59.
[25] Bruns OT, Bischof TS, Harris DK, et al. Next-generation in vivo optical imaging with short-wave infrared quantum dots. Nat Biomed Eng. 2017; 1: 0056.
[26] Franke D, Harris DK, Chen O, et al. Continuous injection synthesis of indium arsenide quantum dots emissive in the short-wavelength infrared. Nat Commun. 2016; 7: 12749.
[27] Zhu CN, Jiang P, Zhang ZL, et al. Ag_2Se quantum dots with tunable emission in the second near-infrared window. ACS Appl Mater Interfaces. 2013; 5: 1186-9.
[28] Wang R, Li X, Zhou L, et al. Epitaxial seeded growth of rare-earth nanocrystals with efficient 800 nm near-infrared to 1525 nm short-wavelength infrared downconversion photoluminescence for in vivo bioimaging. Angew Chem Int Ed. 2014; 53: 12086-90.
[29] Naczynski DJ, Sun C, Turkcan S, et al. X-ray-induced shortwave infrared biomedical imaging using rare-earth nanoprobes. Nano Lett. 2015; 15: 96-102.
[30] Wang R, Zhou L, Wang W, et al. In vivo gastrointestinal drug-release monitoring through second near-infrared window fluorescent bioimaging with orally delivered microcarriers. Nat Commun. 2017; 8: 14702.
[31] Zhong Y, Ma Z, Zhu S, et al. Boosting the down-shifting luminescence of rare-earth nanocrystals for biological imaging beyond 1500 nm. Nat Commun. 2017; 8: 737.
[32] Schnermann MJ. Chemical biology: Organic dyes for deep bioimaging. Nature. 2017; 551: 176-77.
[33] Qian G, Dai B, Luo M, et al. Band Gap Tunable, Donor−Acceptor−Donor Charge-Transfer Heteroquinoid-Based Chromophores: Near Infrared Photoluminescence and Electroluminescence. Chem Mater. 2008; 20: 6208-16.
[34] Antaris AL, Chen H, Cheng K, et al. A small-molecule dye for NIR-II imaging. Nat Mater. 2016; 15: 235-42.
[35] Zhang XD, Wang H, Antaris AL, et al. Traumatic Brain Injury Imaging in the Second Near-Infrared Window with a Molecular Fluorophore. Adv Mater. 2016; 28: 6872-9.
[36] Cheng K, Chen H, Jenkins CH, et al. Synthesis, Characterization, and Biomedical Applications of a Targeted Dual-Modal Near-Infrared-II Fluorescence and Photoacoustic Imaging Nanoprobe. ACS Nano. 2017; 11: 12276-91.
[37] Antaris AL, Chen H, Diao S, et al. A high quantum yield molecule-protein complex fluorophore for near-infrared II imaging. Nat Commun. 2017; 8: 15269.
[38] Carr JA, Franke D, Caram JR, et al. Shortwave infrared fluorescence imaging with the clinically approved near-infrared dye indocyanine green. Proc Natl Acad Sci U S A. 2018; 115: 4465-70.
[39] Starosolski Z, Bhavane R, Ghaghada KB, et al. Indocyanine green fluorescence in second near-infrared (NIR-II) window. Plos One. 2017; 12: e0187563.
[40] Zhu S, Hu Z, Tian R, et al. Repurposing cyanine NIR-I dyes accelerates clinical translation of near-infrared-II (NIR-II) bioimaging. Adv. Mater. 2018; 10.1002/adma.201802546
[41] Troyan SL, Kianzad V, Gibbs-Strauss SL, et al The FLARE intraoperative near-infrared fluorescence imaging system: a first-in-human clinical trial in breast cancer sentinel lymph node mapping. Ann Surg Oncol. 2009; 16: 2943-52.
[42] Alander JT, Kaartinen I, Laakso A, et al. A review of indocyanine green fluorescent imaging in surgery. Int J Biomed Imaging. 2012; 2012: 940585.
[43] Qian G, Wang ZY. Design, synthesis, and properties of benzobisthiadiazole-based donor –π– acceptor –π– donor type of low-band-gap chromophores and polymers. Can J Chem. 2010; 88: 192-201.
[44] Qi J, Han J, Zhou X, et al. Optimization of Broad-Response and High-Detectivity Polymer Photodetectors by Bandgap Engineering of Weak Donor–Strong Acceptor Polymers. Macromolecules. 2015; 48: 3941-48.
[45] Yao L, Zhang S, Wang R, et al. Highly efficient near-infrared organic light-emitting diode based on a butterfly-shaped donor-acceptor chromophore with strong solid-state fluorescence and a large proportion of radiative excitons. Angew Chem Int Ed. 2014; 53: 2119-23.
[46] Shang H, Fan H, Shi Q, et al. Solution processable D-A-D molecules based on triphenylamine for efficient organic solar cells. Sol Energy Mater Sol Cells. 2010; 94: 457-64.
[47] Qian G, Wang ZY. Near-infrared organic compounds and emerging applications. Chem Asian J. 2010; 5: 1006-29.
[48] Qian G, Gao JP, Wang ZY. Near-infrared chemiluminescence tunable from 900 nm to 1700 nm from narrow-bandgap compounds and polymers. Chem Commun. 2012; 48: 6426–28.
[49] Semonin OE, Johnson JC, Luther JM, et al. Absolute Photoluminescence Quantum Yields of IR-26 Dye, PbS, and PbSe Quantum Dots. J Phys Chem Lett. 2010; 1: 2445-50.
[50] Hatami S, Wurth C, Kaiser M, et al. Absolute photoluminescence quantum yields of IR26 and IR-emissive Cd(1-x)Hg(x)Te and PbS quantum dots-method- and material-inherent challenges. Nanoscale. 2015; 7: 133-43.
[51] Yang Q, Hu Z, Zhu S, et al. Donor Engineering for NIR-II Molecular Fluorophores with Enhanced Fluorescent Performance. J Am Chem Soc. 2018; 140: 1715-24.
[52] Zhu S, Yang Q, Antaris AL, et al. Molecular imaging of biological systems with a clickable dye in the broad 800- to 1,700-nm near-infrared window. Proc Natl Acad Sci U S A. 2017; 114: 962-67.
[53] Sun Y, Qu C, Chen H, et al. Novel benzo-bis(1,2,5-thiadiazole) fluorophores for in vivo NIR-II imaging of cancer. Chem Sci. 2016; 7: 6203-07.
[54] Sun Y, Ding M, Zeng X, et al. Novel bright-emission small-molecule NIR-II fluorophores for in vivo tumor imaging and image-guided surgery. Chem Sci. 2017; 8: 3489-93.
[55] Cosco ED, Caram JR, Bruns OT, et al. Flavylium Polymethine Fluorophores for Near- and Shortwave Infrared Imaging. Angew Chem Int Ed. 2017; 56: 13126-29.
[56] Cao W, Sletten EM. Fluorescent Cyanine Dye J-Aggregates in the Fluorous Phase. J Am Chem Soc. 2018; 140: 2727-30.
[57] Tao Z, Hong G, Shinji C, et al. Biological imaging using nanoparticles of small organic molecules with fluorescence emission at wavelengths longer than 1000 nm. Angew Chem Int Ed. 2013; 52: 13002-6.
[58] Prosposito P, Casalboni M, De Matteis F, et al. IR-Luminescent Molecules in Hybrid Materials. J Solgel Sci Technol. 2003; 26: 909-13.
[59] Li B, Lu L, Zhao M, et al. An Efficient 1064 nm NIR-II Excitation Fluorescent Molecular Dye for Deep-Tissue High-Resolution Dynamic Bioimaging. Angew Chem Int Ed. 2018; 57: 7483-87.
[60] Hong G, Diao S, Chang J, et al. Through-skull fluorescence imaging of the brain in a new near-infrared window. Nat Photonics. 2014; 8: 723-30.
[61] Qi J, Sun C, Zebibula A, et al. Real-Time and High-Resolution Bioimaging with Bright Aggregation-Induced Emission Dots in Short-Wave Infrared Region. Adv Mater. 2018; 30: e1706856.
[62] Xu G, Yan Q, Lv X, et al. Imaging of Colorectal Cancers Using Activatable Nanoprobes with Second Near-Infrared Window Emission. Angew Chem Int Ed. 2018; 57: 3626-30.
[63] Rosenthal EL, Warram JM, de Boer E, et al. Safety and Tumor Specificity of Cetuximab-IRDye800 for Surgical Navigation in Head and Neck Cancer. Clin Cancer Res. 2015; 21: 3658-66.
[64] Gao RW, Teraphongphom N, de Boer E, et al. Safety of panitumumab-IRDye800CW and cetuximab-IRDye800CW for fluorescence-guided surgical navigation in head and neck cancers. Theranostics. 2018; 8: 2488-95.
[65] Li D, Zhang J, Chi C, et al. First-in-human study of PET and optical dual-modality image-guided surgery in glioblastoma using (68)Ga-IRDye800CW-BBN. Theranostics. 2018; 8: 2508-20.
[66] Vinegoni C, Botnaru I, Aikawa E, et al. Indocyanine green enables near-infrared fluorescence imaging of lipid-rich, inflamed atherosclerotic plaques. Sci Transl Med. 2011; 3: 84ra45.
[67] Hagenbuch B. Drug uptake systems in liver and kidney: a historic perspective. Clin Pharmacol Ther. 2010; 87: 39-47.
[68] Cilliers C, Nessler I, Christodolu N, et al. Tracking Antibody Distribution with Near-Infrared Fluorescent Dyes: Impact of Dye Structure and Degree of Labeling on Plasma Clearance. Mol Pharm. 2017; 14: 1623-33.
[69] Yu M, Liu J, Ning X, et al. High-contrast Noninvasive Imaging of Kidney Clearance Kinetics Enabled by Renal Clearable Nanofluorophores. Angew Chem Int Ed. 2015; 54: 15434-8.
[70] Choi HS, Gibbs SL, Lee JH, et al. Targeted zwitterionic near-infrared fluorophores for improved optical imaging. Nat Biotechnol. 2013; 31: 148-53.

[71] Choi HS, Nasr K, Alyabyev S, et al. Synthesis and in vivo fate of zwitterionic near-infrared fluorophores. Angew Chem Int Ed. 2011; 50: 6258-63.
[72] Kang H, Gravier J, Bao K, et al. Renal Clearable Organic Nanocarriers for Bioimaging and Drug Delivery. Adv Mater. 2016; 28: 8162-68.
[73] Lane LA, Xue R, Nie S. Emergence of two near-infrared windows for in vivo and intraoperative SERS. Curr Opin Chem Biol. 2018; 45: 95-103.
[74] Zhou C, Hao G, Thomas P, et al. Near-infrared emitting radioactive gold nanoparticles with molecular pharmacokinetics. Angew Chem Int Ed. 2012; 51: 10118-22.
[75] He S, Song J, Qu J, et al. Crucial breakthrough of second near-infrared biological window fluorophores: design and synthesis toward multimodal imaging and theranostics. Chem Soc Rev. 2018; 47: 4258-78.
[76] Sampath L, Kwon S, Hall MA, et al. Detection of Cancer Metastases with a Dual-labeled Near-Infrared/Position Emission Tomography Imaging Agent. Transl Oncol. 2010; 3: 307-17.
[77] Chi C, Du Y, Ye J, et al. Intraoperative imaging-guided cancer surgery: from current fluorescence molecular imaging methods to future multi-modality imaging technology. Theranostics. 2014; 4: 1072-84.
[78] Tian R, Jacobson O, Niu G, et al. Evans Blue Attachment Enhances Somatostatin Receptor Subtype-2 Imaging and Radiotherapy. Theranostics. 2018; 8: 735-45.
[79] Chen H, Tong X, Lang L, et al. Quantification of Tumor Vascular Permeability and Blood Volume by Positron Emission Tomography. Theranostics. 2017; 7: 2363-76.